# Fluorescence detection at the atom shot noise limit for atom interferometry

Rocco, E; Palmer, R N; Valenzuela, T; Boyer, V; Freise, A; Bongs, K

*DOI:*
10.1088/1367-2630/16/9/093046



*Document Version*
Publisher's PDF, also known as Version of record

*Citation for published version (Harvard):*
Rocco, E, Palmer, RN, Valenzuela, T, Boyer, V, Freise, A & Bongs, K 2014, 'Fluorescence detection at the atom shot noise limit for atom interferometry', *New Journal of Physics*, vol. 16, no. 9, 093046. https://doi.org/10.1088/1367-2630/16/9/093046

Fluorescence detection at the atom shot noise limit for atom interferometry



2014 New J. Phys. 16 093046

(http://iopscience.iop.org/1367-2630/16/9/093046)

New Journal of Physics
The open access journal at the forefront of physics
Deutsche Physikalische Gesellschaft DPG | IOP Institute of Physics

# Fluorescence detection at the atom shot noise limit for atom interferometry

**E Rocco, R N Palmer, T Valenzuela[1], V Boyer, A Freise and K Bongs**
The School of Physics and Astronomy, University of Birmingham, Edgbaston, Birmingham B15 2TT, UK
E-mail: e.rocco@bham.ac.uk

Received 28 April 2014, revised 18 July 2014
Accepted for publication 5 August 2014
Published 25 September 2014
*New Journal of Physics* **16** (2014) 093046
doi:10.1088/1367-2630/16/9/093046

**Abstract**
Atom interferometers (AIs) are promising tools for precision measurement with applications ranging from geophysical exploration and tests of the equivalence principle of general relativity to the detection of gravitational waves. Their optimal sensitivity is ultimately limited by their detection noise. We review resonant and near-resonant methods to detect the atom number of the interferometer outputs, and we theoretically analyze the relative influence of various scheme dependent noise sources and the technical challenges affecting the detection. We show that for the typical conditions under which an AI operates, simultaneous fluorescence detection with a charge-coupled device sensor is the optimal imaging scheme. We extract the laser beam parameters such as detuning, intensity, and duration required for reaching the atom shot noise limit.

Keywords: atom interferometry, fluorescence detection, atom shot noise limit, atom cloud imaging

## 1. Introduction

In the late eighties the invention of laser cooling [1] pushed the development of atom interferometry (AI) [2]. Since then, atom interferometers (AIs) have been used in basic science

[1] Present address: RAL Space, Science and Technology Facilities Council, Rutherford Appleton Laboratory, Harwell, Didcot, Oxfordshire, OX11 0QX, UK.

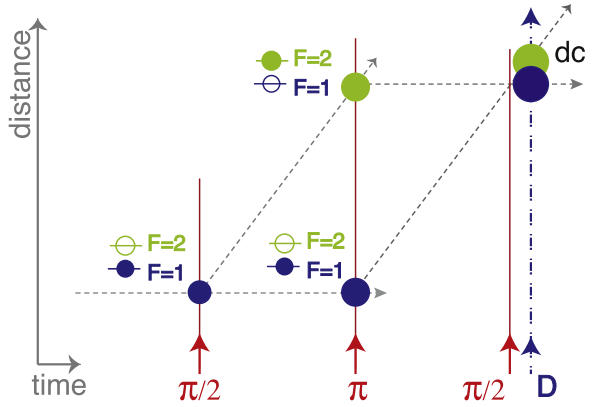


**Figure 1.** Working schematics for a light pulse atom interferometer with $\pi$ and $\pi/2$ the beam pulses, 'D' the detection beam, and 'dc' the output atom clouds.

for the measurement of the $\hbar/m$ ratio [3], the fine structure constant [4], and the Newtonian gravitational constant [5, 6], as well as for tests of the equivalence principle of general relativity (EP) [7, 8]. Fundamental science applications based on AI have been proposed such as very precise space EP tests [9], low frequency gravitational wave detectors [10], and laboratory tests of dark energy [11]. In applied science, research and development efforts have been focused on the development of inertial and gravitational sensors based on AIs such as accelerometers [12], gyroscopes [13], gravimeters [14], and gravity gradiometers [15]. These quantum sensors will allow more precise measurements of Earth's gravitational potential for climate-change studies, novel mapping of city undergrounds, and searches for new mineral and oil resources.

AIs rely on the optical control of the atom wave functions through the precise use and timing of laser pulses (see figure 1) and on the translation of the AI differential phase $\phi$ into the population unbalance among the possible energy, or momentum state, of the output cloud atoms. In the case of an AI as illustrated in figure 1, the expected renormalized population imbalance $\zeta$ is given by $(N_1 - N_2)/(N_1 + N_2)$, with $N_1$ and $N_2$ the atom numbers of the two AI output clouds; it is a function of $\phi$. The population unbalance and therefore the AI differential phase are evaluated by measuring the output cloud atom numbers during the final detection sequence.

The detection noise in the atom number measurement is one of the main noise sources limiting the sensitivity of AIs. Even if other noise sources might be present, such as wavefront distortion or phase noise in the AI laser pulses, the ability to reduce the detection noise of the cloud atom number down to the atom shot noise limit is necessary to build AIs that work at their optimal design sensitivity.

Some previous theoretical and experimental work has been carried out to examine the conditions to reach optimal detection for matter–wave optics [16, 17]. However, a detailed analysis of the errors affecting the detection noise of AIs, particularly with a large atom number but small optical depth, is currently missing. In section 2 we study the technical challenges and error sources affecting fluorescence, absorption, and dark imaging detection for different detection sequences, with the scope to identify a detection method which could be limited by the atom shot noise only. In sections 3–4 we show how simultaneous fluorescence detection of both output clouds by charge-coupled device (CCD) imaging poses less stringent technical requirements on the detection beam noise, and we identify the optimal detection parameters

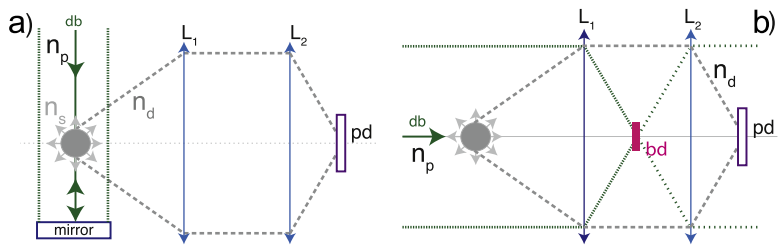


**Figure 2.** Detection scheme for: (a) fluorescence and (b) absorption and dark imaging, with the last differing only by the presence of the blocking beam disk 'bd'. The photodetector is 'pd,' 'db' the detection beam, and $L_1$ and $L_2$ a focusing lens system. The detected photon number is $n_d$, $n_p$ is the incoming photon number, and $n_s$ is the scattered photon number.

such as detection time, detuning, saturation ratio, CCD pixel size, and number to reach the atom shot noise limit.

## 2. Near resonant detection methods for atom interferometry

AIs typically operate with large atom numbers in the range of $\approx 10^5$–$10^7$ but optically thin clouds with optical depths $\tau$ between a few $10^{-3}$ and a few $10^{-2}$. To detect the atom number of these output clouds, the most often adopted detection methods in AI are near resonance ones, where a detection laser beam illuminates the atoms with a laser frequency that is near the resonant frequency of the atomic transition to interrogate. The atom number is then detected by measuring the scattering dispersion or absorption of photons as in fluorescence, absorption, or dark imaging detection. Other possible detection methods are far off resonance ones, which are based on the phase shift and polarization rotation induced by the atoms on the beam photons when these have a frequency far from the interrogated atomic resonance. However, these detection methods are generally not used in AI because they require very high optical densities that cannot be achieved in beam-based or free-fall AIs. Therefore we do not include them in this work.

In the near resonant methods the scattered and transmitted photons (see figure 2) are intercepted by a lens with numerical aperture NA, and then through some optics they are imaged onto a photo detector such as a CCD or a photodiode. Furthermore, in dark-ground imaging, the detection beam is blocked by an additional disk positioned in the centre of the Fourier plane, and only the fluorescence and the diffracted light are imaged on the photodetector [16]. From these measurements, once all the detection parameters are known, the cloud atom number $N$ can be derived.

This estimate of $N$ is affected by a number of noise sources, like atom shot noise and photon shot noise with standard deviations $\sigma_N = \sqrt{N}$ and $\sigma_p = \sqrt{n_d}$, respectively, where $n_d$ is the photon number counted by the photodetector during the detection time. The noises on laser intensity $I$ and frequency $\nu$ of the detection laser beam induce an error on the estimate of $N$ as well. We assume these noises to be Gaussian and with standard deviations $\sigma_I$ and $\sigma_\Delta$, respectively.

The noise optimization of the detection method depends very much on the atom number and the optical depth of the imaged clouds. A typical AI has output clouds characterized by a small optical depth with $\sigma\rho_{2D} \ll 1$ [16], where $\sigma$ is the atomic scattering cross section and $\rho_{2D}$ the column atom density of the cloud along the beam axis. For a spherically symmetric Gaussian density distribution with standard deviation $\sigma_\rho$, the maximum column atom density

along the detection beam optical axis is $\rho_{2D_{max}} = N/(2\pi\sigma_\rho^2)$. In the following, we assume $N$ to be in the range $10^5 - 2 \times 10^7$ and the cloud size $\sigma_\rho$ in the range 1–5 mm, which are typical values for $^{87}$Rb, $^{85}$Rb, $^{133}$Cs, and $^{39}$K AIs [18–22]. The AI large cloud sizes and the corresponding small optical depths are due to the long interrogation time necessary to achieve high enough sensitivities; high atom numbers are detrimental to the efficiency of molasses cooling and result in higher temperatures and therefore in larger final cloud sizes. We also assume an imaging lens with a numerical aperture of NA = 0.2 and the use of $^{87}$Rb atoms. At resonance, e.g. for circularly polarized light, $\sigma$ is $\sigma_0 = 2.9 \times 10^{-13}$ m$^{-2}$ [23]. Under these assumptions, because the optical depths $\tau = \sigma_0\rho_{2D_{max}}$ are in the range of $\approx(2 \times 10^{-3}, 4 \times 10^{-2})$, the hypothesis of small $\tau$ is valid.

Given the assumed small optical depths, we can exclude the dark-ground imaging from the analysis. In fact, for $\sigma\rho_{2D} \ll 1$, the fluorescence signal dominates the coherent diffraction at near-resonance [16], and dark ground imaging is fully equivalent to fluorescence detection.

Absorption imaging is also excluded because of the technical challenges to image enough photons on a CCD and reach the atom shot noise limit. Indeed, only for a minimum number of scattered detected photons $(n_d)_{min}$, the contribution to the detection noise of the atom shot noise $\sigma_N$ dominates over the contribution of the photon shot noise $\sigma_{n_d}$ by a factor $\beta$. The parameter $\beta$ can be freely chosen. For a detection as close as possible to the fundamental limit of atom shot noise, we require $\beta = 3$, for which the total noise on the measured atom number is given at 95% by the atom shot noise. Larger values of $\beta$ are not very beneficial since, for only small gains on the signal-to-noise ratio (SNR), they will impose much stronger constraints on the experimental parameters, as we will show later. For low optical depths, we are now showing that $(n_d)_{min}$ for absorption is much larger than $(n_d)_{min}$ for fluorescence and technically difficult to detect by CCD imaging. In absorption imaging, one usually measures the transmittance $T$ as defined by $n_d/n_p$, with $n_p$ the number of the incoming photons and $n_d$ the photon's number reaching the detector, which is given by [16]:

$$n_d = n_p \exp(-\sigma\rho_{2D}) \approx n_p(1 - kN), \tag{1}$$

with $k = \sigma\rho_{2D}/N$, where $\sigma$ is the scattering cross section (see equation (A.2)). The total noise on the measured transmittance $T$ due to the atom and photon shot noises is equal to $\sigma_T = \sqrt{2\sigma_p + (n_p\kappa)^2\sigma_N^2}$. Considering also that the transmittance $T$ for a cloud with a Gaussian density profile has a minimum value $T_{min} \approx 1 - k_{max}N$ with $k_{max} = \sigma/(2\pi\sigma_\rho^2)$, the atom shot noise contribution to $\sigma_T$ is dominant over the contribution of the photon shot noise by at least a factor $\beta$ only for $n_d > (n_d)_{min} = 2\beta^2/(k_{max}^2 N)$. Under our numerical assumptions, with $\sigma_\rho = 5$ mm and with $N = 10^6$, $(n_d)_{min}$ is $\approx 5.2 \times 10^{11}$, which, assuming a CCD sensor with a maximum pixel well depth of $10^5$ photons/pixel, requires a minimum pixel number of $5.2 \times 10^6$ per cloud to be imaged. For an AI with two or more clouds (as in [9]) to be imaged, CCDs with such a pixel number are not yet easily available on the market.

On the other hand, $(n_d)_{min}$ for fluorescence is easily detectable with a CCD. Indeed, for small optical depths [16], we find that $n_d = \alpha N$, with $\alpha$ a proportionality constant, depending on the atom cross section and the duration and intensity of the probe beam (see equation (A.1)). The total detection noise on $n_d$ for fluorescence is $\sqrt{\sigma_p^2 + \alpha^2\sigma_N^2}$, which, independently of the expression of $\alpha$, has the atom shot noise contribution dominant by a factor $\beta$ over the photon shot noise for $n_d > (n_d)_{min} = N\beta^2$. It is interesting to notice that for fluorescence detection,

$(n_d)_{min}$ increases with the atom number, which is the opposite of what is required for absorption detection. With our assumptions and for fluorescence detection, $(n_d)_{min}$ is $9 \times 10^6$, which requires only a 90 pixel CCD, assuming a pixel well depth of $10^5$ photons/pixel. Another advantage of fluorescence detection over absorption is that, as shown in figure 2, it allows one to implement optical molasses by positioning a retro-reflecting mirror along the beam axis. In particular, we can set up red detuning molasses to avoid the heating of the atoms at resonance, implement Doppler cooling, and so keep them in the detection volume for longer times.

Even if detection with a photodiode is technically simpler than with a CCD and allows shot noise limited absorption detection, using a CCD is still preferable, since it allows one to record the spatial information of the output clouds. This information can be useful for some applications, because it can be used to estimate the angular velocity of the AI [19, 24]. It also allows one to resolve different output clouds if they are simultaneously imaged. From the discussion in this section, we conclude that for AI and CCD imaging, fluorescence is more technically feasible than absorption imaging, which would require very large pixel numbers.

## 3. Sequential versus simultaneous fluorescence detection

Given fluorescence as the chosen detection method, the AI output clouds can be imaged in a sequential or simultaneous way: in sequential imaging, the hyperfine state populations of the atoms in the AI output clouds are estimated in a time sequence one after the other; in simultaneous imaging, the atoms in different hyperfine states are in spatially distinguishable clouds which are imaged at the same time. Sequential imaging is simpler to realize than simultaneous, but, as we discuss in section 3.1.1, because of atom loss to unwanted transitions, it requires a longer interrogation time and is constrained by a maximum allowed laser detuning with respect to the resonance. As we discuss in section 3.1.2, it is also affected by the laser frequency and intensity noise, requiring dedicated detection beam stabilization. As we show in section 3.2, simultaneous fluorescence detection with CCD imaging instead allows one to measure the atom cloud population at the atom shot noise limit with less stringent technical requirements on the stability of the detection-beam parameters.

### *3.1. Limitations of sequential imaging*

In sequential imaging, the AI output clouds are imaged in two ways: if the clouds are spatially separated, they are imaged one after the other as they fall under gravity, illuminated by one detection beam in front a photo detector. In the other method, the superimposed clouds have the atoms in distinct hyperfine ground states, and their populations are imaged one after the other by using different detection beams tuned to different detection frequencies.

*3.1.1. Constraints on detection time and detuning frequency.* In the two-level model of detection (see appendix A), for the example of $^{87}$Rb, the atoms in a hyperfine $F = 2$ ground state cycle through the excited $F' = 3$ state, emitting the photons to be detected by the photodetector. However, in a realistic multi-level model, some atoms might be excited to secondary hyperfine states and then subsequently lost through non-closed transitions. In the case of $^{87}$Rb atoms with the $D_2$ line hyperfine structure represented in figure 3 [23], a detection beam with a frequency red detuned by $\Delta$ with respect to the $F = 2 \rightarrow F' = 3$ transition induces not only the desired

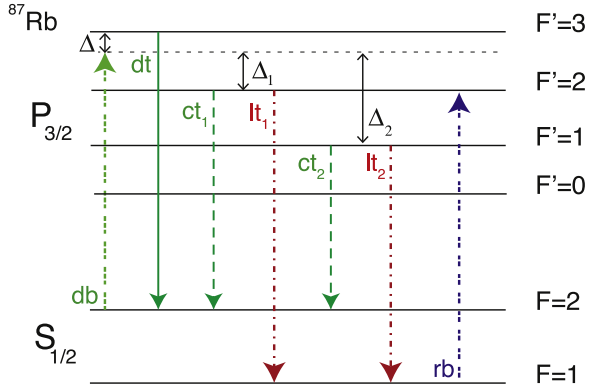


**Figure 3.** Schema of the modeled transitions for the $^{87}$Rb $D_2$ lines. $lt_1$, and $lt_2$ are the loss transitions; 'dt' the detection one; and $ct_1$ and $ct_2$ are closed depumping transitions. The detection beam is 'db,' and 'rb' is the repumper one.

fluorescence transition but also the $F = 2 \rightarrow F' = 2$ and $F = 2 \rightarrow F' = 1$ ones. As represented in figure 3 (dashed red arrow), some of the atoms in these $F' \neq 3$ excited states spontaneously decay to the $F = 1$ ground state, which is decoupled from the detection light. If the AI output state clouds are physically superimposed, a repumper beam cannot be used to cycle back the atoms from the $F = 1$ to the $F = 2$ ground state. In this case, the leakage to the $F = 1$ state is effectively an atom loss for the AI population estimation and modifies the number of scattered photons versus time $n_s(t)$ of the two-level atom. By modifying $n_s(t)$, this atom loss implies an increase of the minimum detection time $\Delta t_{min}$ as a function of the red detuning $\Delta$, setting constraints on the allowed $\Delta$ and saturation ratio $s = I/I_{sat}$ to reach the atom shot noise limit, where $I_{sat}$ is the saturation intensity as defined [23, 25]. In the model which includes atom loss through non-closed transitions, $\Delta t_{min}$ is given by:

$$\Delta t_{min} = \frac{I_{sat}}{I}\frac{2}{\Gamma\gamma_{lost}}\log\left[\left(1 - \frac{\gamma_{lost}}{\gamma_d}\frac{(n_s)_{min}}{N}\right)^{-1}\right], \tag{2}$$

where $\Gamma$ is the natural line-width (FWHM) of the considered transitions, which, in the case of $^{87}$Rb, is $2\pi \times 6.06$ MHz [23]. The parameters $\gamma_d = \gamma(\Delta)$ and $\gamma_{lost} = \sum_i \gamma(\Delta_i)\,\mathrm{br}_i$ are respectively proportional to the scattering cross sections of the detection fluorescence transition and of all the lost non-closed transitions. The function $\gamma(\Delta)$ is the function given by:

$$\gamma(\Delta) = \left(1 + \frac{I}{I_{sat}} + 4\frac{\Delta^2}{\Gamma^2}\right)^{-1}, \tag{3}$$

where $\Delta_i = \Delta_{di} - \Delta$ is the detuning with respect to the non-detection hyperfine transitions, and $\Delta_{\mathrm{di}}$ is the frequency difference of these transitions with respect to the detection one. Finally, $\mathrm{br}_i$ is the spontaneous emission branching ratio to non-closed transitions (see appendix C). From section 2, $(n_s)_{min}$ is given by $(n_d)_{min}/\Omega$, with $(n_d)_{min} = N\beta^2$, where $\Omega \approx \mathrm{NA}^2/4$ is the fraction of solid angle intercepted by the imaging lens of numerical aperture NA.

In some cases the requirements on the photon shot noise are too strict, and $\Delta t_{min}$ does not exist because all the atoms are lost to non-closed transitions before scattering enough photons to reach the atom shot noise limit. For a given choice of $\beta$ and saturation ratio $s$, this happens for

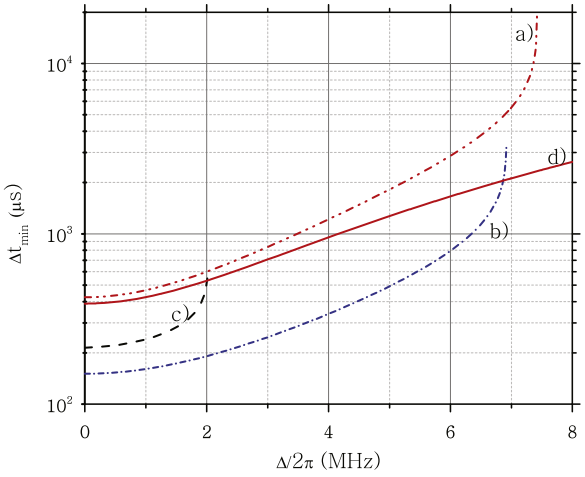


**Figure 4.** Minimum detection time $\Delta t_{min}$ for $^{87}$Rb for different saturation ratios $s$: 'a', 'b', and 'c' refer to $s$ of 0.2, 1, and 6. The continuous line 'd' is $(\Delta t_{min})_{2l}$ for the two-atom level model for $s = 0.2$.

detuning larger than some detuning $\Delta_{\max}$, which is found by numerically solving the following equation in $\Delta_{\max}$:

$$\frac{\beta^2}{\Omega} = \frac{\gamma_d(\Delta_{max})}{\gamma_{lost}(\Delta_{max})}. \tag{4}$$

Equivalently, for a chosen $\beta$ and detuning parameter $\Delta$, there is a maximum allowed saturation ratio $s_{max}$ to reach the atom shot noise limit.

For the alkali atoms, small saturation ratio $s$ and small detuning $\Delta$, $\gamma_{lost}/\gamma_d$ is of the order of $10^{-3}$. Under these conditions $\Delta t_{min}$ can be described by:

$$\Delta t_{min} \approx (\Delta t_{min})_{2l}\left[1 + \frac{\gamma_{lost}}{\gamma_d}\frac{\beta^2}{2\Omega}\right], \tag{5}$$

with $(\Delta t_{min})_{2l}$ the minimum detection time to reach the atom shot noise limit for the two-level model without atom loss (see appendix A), given by:

$$(\Delta t_{min})_{2l} = \frac{2}{\Gamma}\frac{I_{sat}}{I}\frac{1}{\gamma_d}\frac{\beta^2}{\Omega}. \tag{6}$$

Assuming NA = 0.2 and $\beta = 3$, at resonance and for saturation ratio $s = 0.2$, $\Delta t_{min}$ is ≈6% larger than $(\Delta t_{min})_{2l}$ but becomes much larger for increasing red detuning $\Delta$ and $s$, e.g., up to a factor of three for $\Delta \approx 1.2\,\Gamma$ and $s = 2$, because more atoms are lost to non-closed transitions. Under our numerical assumptions, in figure 4 we plot $\Delta t_{min}$ versus the red detuning $\Delta$ with respect to the $F' = 3$ hyperfine level of $^{87}$Rb for different saturation ratios $s$. The branching ratio to the non-closed transition is 50% and 83%, respectively, for the hyperfine level $F' = 2$ and $F' = 1$ (see table C1). Figure 4 shows that, for red detuning $\Delta \geqslant 2\pi \times 7.4$ MHz, it is impossible to reach atom shot noise detection, because all the atoms are lost to non-closed transitions before reaching the atom shot noise limit. For comparison, we plot as well the curve for the simple two-level system of equation (6) as a continuous line, which shows a much reduced

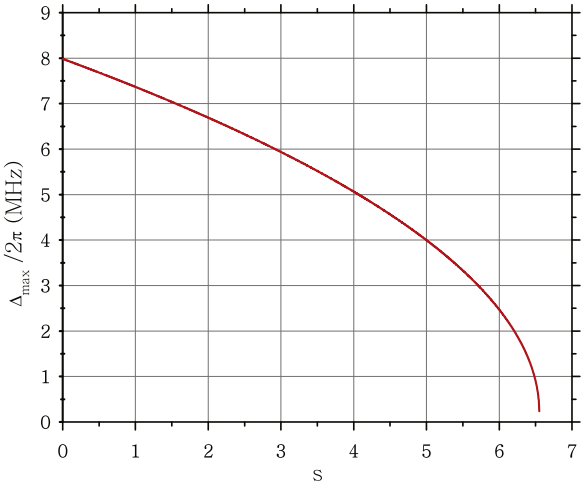


**Figure 5.** Maximum detuning as a function of the saturation ratio $s$ for $^{87}$Rb.

detection time for large detuning. In figure 5 we plot the maximum allowed red detuning $\Delta_{\max}$ as a function of the saturation ratio $s$ showing that, for large detunings, it is necessary to have a low intensity detection beam to reach the atom shot noise limit. The same figure means that, as a function of the detuning, there is a maximum allowed saturation ratio. A detection sequence based on simultaneous imaging with a repumper beam does not pose such constraints on the maximum allowed red detuning and, with respect to the simple two-level model and for a given detection time, requires a smaller saturation ratio to reach the atom shot noise limit (compare, e.g., figures 4 and 8). Such a simultaneous imaging sequence is thus preferable to sequential imaging.

*3.1.2. Constraints on frequency and power noise of detection beam.* The laser frequency and power noises also induce noise on the detection. We show now that for sequential detection, the requirements on these noise sources to reach the atom shot noise limit can be technically challenging and make simultaneous detection a preferable alternative detection method (see section 3.2). If $\sigma_\Delta$ is the standard deviation of the laser frequency noise between the readouts of the output clouds, its induced error on $n_d$, $(\sigma^2_{n_d})_{\sigma_\Delta}$ is given by:

$$\left(\sigma^2_{n_d}\right)_{\sigma_\Delta} = \left(\frac{\partial\alpha}{\partial\Delta}N\right)^2\sigma^2_\Delta + \left(\frac{\partial^2\alpha}{\partial\Delta^2}N\right)^2\frac{\sigma^4_\Delta}{2}, \tag{7}$$

with the second order derivative of $\alpha$ with respect to $\Delta$ [26] being the dominant term for low detuning. The constraints on the laser noises are derived from their induced error on the detected photons $n_d$. In fact, by requiring that $\alpha\sigma_N > \beta(\sigma_{n_d})_{\sigma_\Delta}$, the constraints on $\sigma_\Delta$ to reach the atom shot noise limit are given for small detuning $\Delta$ by:

$$\sigma_\Delta < \Gamma\frac{\sqrt{1+\frac{I}{I_{sat}}}}{4\sqrt{\beta}\,(2N)^{1/4}} \tag{8}$$

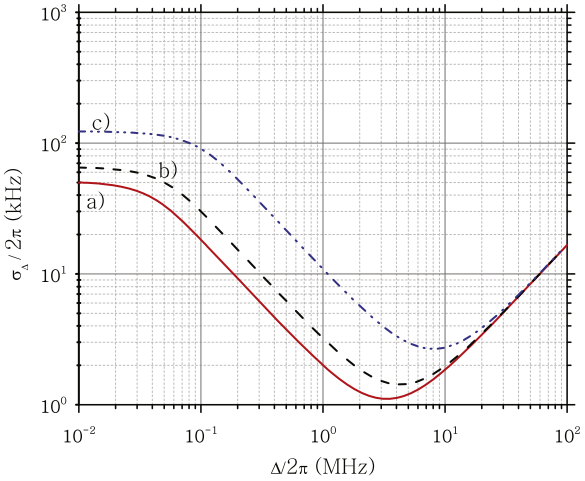


**Figure 6.** Requirements on the laser frequency noise $\sigma_\Delta$ versus the detuning frequency $\Delta$ for $T = 1$ (s) for different values of the saturation ratio: 'a', 'b', and 'c' refer to values of $s$ of 0.2, 1, and 6, respectively.

and for larger $\Delta$ by:

$$\sigma_\Delta < \frac{1}{\beta\sqrt{N}}\frac{\Gamma^2}{8\Delta}\left(1 + 4\frac{\Delta^2}{\Gamma^2} + \frac{I}{I_{sat}}\right). \tag{9}$$

Similarly, the constraints on the fractional standard deviation $\sigma_I/I$ of the laser intensity noise between the output readings to reach the atom shot noise limit can be derived, and are given by:

$$\frac{\sigma_I}{I} < \frac{1}{\beta\sqrt{N}}\left(1 + \frac{I}{I_{sat}}\frac{1}{1 + 4\frac{\Delta^2}{\Gamma^2}}\right). \tag{10}$$

In figure 6 we plot the maximum laser frequency noise $\sigma_\Delta$ for $^{87}$Rb with the numerical assumptions of section 2. In this figure, the curve on the requirements on $\sigma_\Delta$ is mainly given by the first derivative of $\alpha$ in $\Delta$, which has a local maximum in correspondence to the inflection point of $\alpha$ as a function of $\Delta$. Considering our numerical assumptions, to reach the atom shot noise limit, $|\sigma_I/I|$ has to be smaller than 0.04% for zero detuning and 0.033% for large detuning.

Even if a long detection time works effectively as a low pass filter, which averages out the high frequency noise of the detection beam, the low frequency components still affect the detection. These requirements on laser frequency and intensity noise need electronic stabilization, and it has already been done in some experiments [15]. This electronic stabilization, however, can prove to be technically challenging, because the relative long time between the detection pulses requires stabilization at low frequencies, where technical noise tends to dominate.

Therefore, alternative approaches should be explored to reduce these laser noise requirements and to allow short detection times.

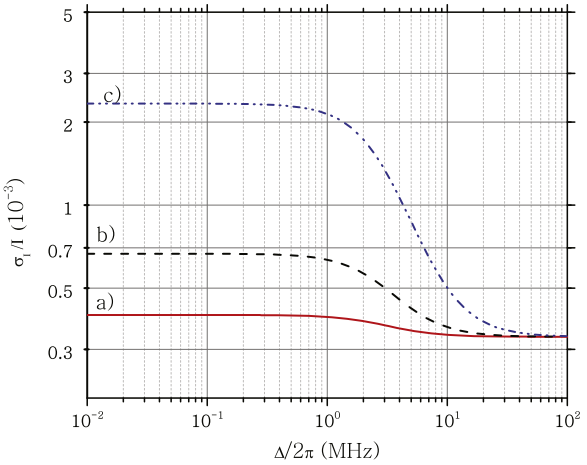


**Figure 7.** Requirements on the fractional standard deviation $\sigma_I/I$ for the different values of the saturation ratio: 'a', 'b', and 'c' refer to the value of $s$ of 0.2, 1, and 6 respectively.

### *3.2. Advantages and constraints of simultaneous imaging*

An alternative approach to detect the output clouds of the AI is to image them all at the same time with a common probe beam. During this simultaneous imaging, the output clouds have to be separated in space to be resolved. Very cold atom clouds could have a momentum spread in the beam splitting direction of the AI small enough that the output clouds will move apart along diverging trajectories and, after some time, become distinguishable. Otherwise, for warmer clouds, state-selective optical molasses can be used to control the motion of the different output clouds and separate them just before detection. During detection, a repumper beam is also used to transfer all the atoms of the output clouds to the same hyperfine ground level as shown in figure 3 so that a common detection beam can be used to detect both clouds. The use of this repumper beam prevents any atom loss through non-closed transitions, as it happens for sequential imaging, and decreases the minimum detection time $\Delta t_{min}$ required to reach the atom shot noise limit. Simultaneous imaging introduces a new noise source associated with cross cloud shadowing (see figure 9), which, however, we show in section 3.2.2, still allows one to reach the atom shot noise limit. Simultaneous imaging does not require as much laser stabilization as sequential imaging and results in a less constrained detection scheme. Because the AI phase is a function of the population unbalance between the AI outputs $\zeta$ and therefore is a relative measurement, the additional complexity of using a repumper beam comes with the advantage that simultaneous imaging allows common mode rejection of the effects of the laser frequency and intensity noises of the detection and repumper beams in the AI phase estimate.

*3.2.1. Reduced constraints on detection time.* Simultaneous imaging, thanks to the repumper beam, can be modeled with the simple two-level atom (see appendix A) and has its minimum detection time $(\Delta t_{min})_{2l}$, given by equation (6), which does not depend on the number of atoms to detect. For example, with the assumptions of section 2 and a saturation ratio $s = 0.2$, $(\Delta t_{min})_{2l}$ is $\approx$400 $\mu$s for zero detuning and, as shown in figure 8, increases with the detuning but becomes smaller for larger saturation ratios.

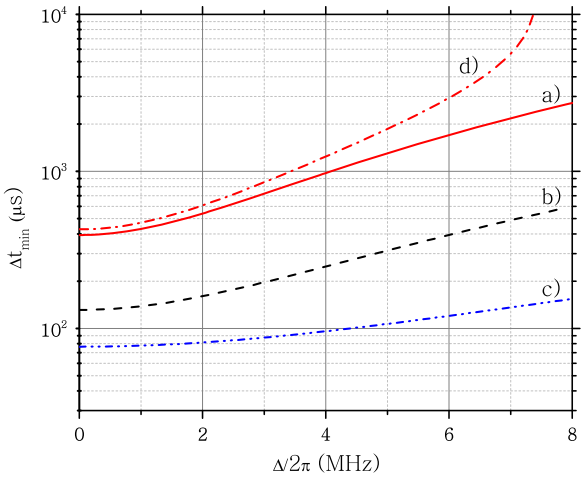


**Figure 8.** Minimum detection time $(\Delta t_{min})_{2l}$ for different saturation ratios $s$: 'a', 'b', and 'c' refer to the values of $s$ of 0.2, 1, and 6, respectively. The continuous line 'd' is $\Delta t_{min}$ for the two-level atom model with losses for $s = 0.2$.

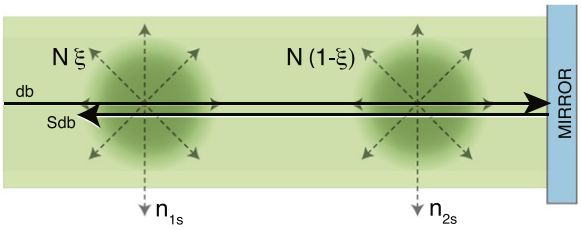


**Figure 9.** Simultaneous readout of two clouds. The detection beam is 'bd'; 'Sdb'; the shadowed detection beam; and $n_{1s}$ and $n_{2s}$ the scattered photon number.

*3.2.2. No constraints from cross cloud shadowing.* In simultaneous imaging, the output clouds share the same detection beam and, as shown in figure 9, cast shadows onto each other. These shadows effectively reduce the number of scattered photons with respect to the shadow-free case, introducing a systematic error. The systematic error on the estimate of the population unbalance between the two AI output cloud $\zeta$, induced by the cross cloud shadowing $\delta_\zeta$ is given by the difference between the 'real' value $\zeta$ and the measured one. This measured population unbalance is given by $\zeta_m = (n_{1\,s} - n_{2\,s})/(n_{1\,s} + n_{2\,s})$, with $n_{1\,s}$ and $n_{2\,s}$ the photons scattered from the first and second output cloud. This approach to estimate $\zeta$ cancels out the effect of the atom number fluctuations between experimental runs, hence reducing the overall phase noise. For small optical depths, $\delta_\zeta$ is a function of the relative atom number of one output cloud $\xi = N_1/N$ with respect to the total atom number $N = N_1 + N_2$ and is given by (see appendix B):

$$\delta_\zeta = -2\Lambda \frac{\xi(1-\xi)(1-2\xi)}{1-\tau+\Lambda(1-\xi(1-\xi))}, \tag{11}$$

where $\tau$ is twice the optical depth associated with the maximum column density $\rho_{2D_{max}}$ and $\Lambda$ is defined in appendix B. In figure 10, for the assumptions of section 2, with $\sigma_\rho = 5$ mm, $N = 3 \times 10^6$, $\Delta = 0$, and $s = 0.2$, we plot the error on the population unbalance $\delta_\zeta$ in unit of the error on $\zeta$ due to the atom shot noise only, $(\sigma_\zeta)_{\sqrt{N}}$, versus the values of $\xi$. The error $(\sigma_\zeta)_{\sqrt{N}}$ is

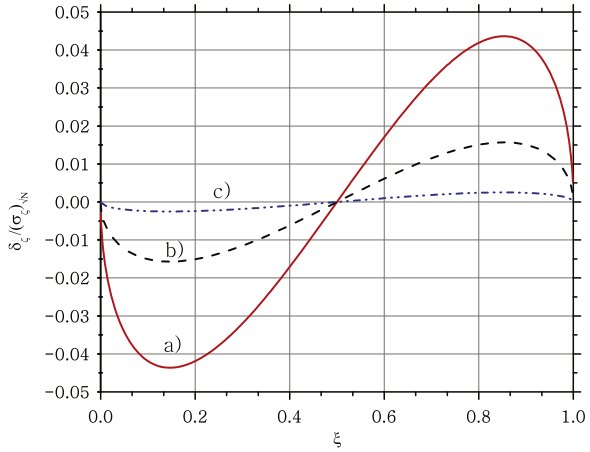


**Figure 10.** Error on the population unbalance $\delta_\zeta$ in unit of the error on $\zeta$, due to the atom shot noise $(\sigma_\zeta)_{\sqrt{N}}$ as a function of $\xi$ and of the saturation ratio $s$ on resonance: 'a,' 'b,' and 'c' refer to the values of $s$ of 0.2, 1, and 4, respectively.

itself a function of $\xi$ and equal to $2\sqrt{\xi(1-\xi)/N}$. The plotted function $\delta_\zeta/(\sigma_\zeta)_{\sqrt{N}}$ has a local maximum at $\xi \approx 0.15$, which shows that the cross-cloud shadowing induced error is just ≈4% of the error coming from the atom shot noise. Cross cloud shadowing therefore does not substantially limit the detection.

To conclude, as discussed above, simultaneous cloud detection is an alternative detection method to the sequential fluorescence imaging, which allows greater flexibility in the detection parameter choices to reach the atom shot noise limit. Indeed, simultaneous imaging does not have constraints that are as strong on the detection frequency and intensity noises because of their common mode rejection; furthermore, simultaneous imaging does not pose any limitation on the maximum allowed red detuning, and it requires a smaller interrogation time or saturation ratio for a shot noise limited detection.

## 4. CCD as imaging sensor for simultaneous imaging

The previous analysis assumed the choice of CCD imaging over photodiode imaging. Indeed, CCD imaging allows one to record the spatial information of the output clouds. As shown below, this spatial information relaxes the requirements on the minimum distance between the output clouds to avoid cross readouts down to the atom shot noise limit. Furthermore, as shown recently [19, 24], the recorded spatial information can be used to characterize velocity-dependent phase shifts in single shot measurements that are visible as a phase shear across the clouds, either to improve AI sensitivity or to design new measurement schemes. For example, phase shear was used by [19] to build an AI gyrocompass sensing two rotations and one acceleration in a single measurement and to determine the Earth's rotation rate with high precision.

### *4.1. CCD to record the cloud spatial information*

In simultaneous imaging, the output clouds, even if they are physically separated, have the tails of their distribution partially overlapped. If the spatial information of the clouds is not

preserved, but only the volume integrals of the photon number are recorded (e.g., with a single photodiode), this cloud overlap induces a systematic error on the population measurements. This error is smaller than the atom shot noise contribution by a factor $\beta$ only if the output cloud centers are at a distance larger than $d_{min}(\beta)$, which can be large and technically difficult to achieve. The spatial information recorded by a CCD can instead be used to spatially fit the atom cloud distribution and so estimate their population without introducing the previous systematic error. To derive an initial estimate, we assume here thermal clouds with Gaussian density distributions at the AI output after having expanded from a very small initial volume at the AI input; otherwise, for Bose–Einstein condensates or velocity-selected clouds, the following calculations will have to be modified accordingly. Thus for two thermal clouds imaged in two semi planes by a photodiode or photo multiplier with equal $\sigma_\rho$ and total number $N/2$, $d_{min}$ is given by:

$$d_{min} = 2\sqrt{2}\,\sigma_\rho\,\mathrm{erf}^{-1}\left(\frac{2\sqrt{2}}{\beta\sqrt{N}}\right), \tag{12}$$

where $\mathrm{erf}^{-1}$ is the inverse of the error function. For our numerical assumptions, the previous equation can be approximated with:

$$d_{min} \approx 2\sigma_\rho\sqrt{\zeta - \ln(\zeta)}\,, \tag{13}$$

with

$$\zeta = \ln(2/\pi) - 2\ln\left(\frac{2\sqrt{2}}{\beta\sqrt{N}}\right). \tag{14}$$

For $N = 10^6$, with $\sigma_\rho = 5$ mm and our assumptions on $\beta$, $d_{min}$ is equal to $6.6\sigma_\rho$, or 3 cm, which for certain applications can be too restrictive.

Therefore, for simultaneous cloud detection, CCD imaging, because it does not require output clouds separated by a large distance and allows one to characterize velocity-dependent phase shifts across them [19, 24], is preferable over an imaging method not recording the spatial information, such as a photodiode or a photomultiplier.

### *4.2. CCD requirements*

Given some CCD parameters such as the pixel well depth $n_w$, the pixel readout noise $\sigma_{px}$, the standard deviation of the dark signal per second $\varsigma_{dk}$, pixel binning number $m$, and the quantum efficiency $\mu$, we identify the minimum and maximum CCD pixel numbers to achieve the atom shot noise limit. In fact, a CCD needs to have at least $(N_{\mathrm{CCD}})_{min}$ pixels to record the fluorescence signal $(n_d)_{min}$:

$$\left(N_{\mathrm{CCD}}\right)_{min} = \frac{N\beta^2}{n_w m}. \tag{15}$$

The maximum pixel number $(N_{\mathrm{CCD}})_{max}$ for a detection time $\Delta t$ is instead given by:

$$\left(N_{\mathrm{CCD}}\right)_{max} = N\beta^2\mu^2\left(\frac{\sigma_{px}^2}{m} + \varsigma_{dk}^2\Delta t^2\right)^{-1}. \tag{16}$$

This expression for $(N_{\mathrm{CCD}})_{max}$ has been obtained by requiring that the total readout noise, $\sigma_{\mathrm{CCD}}^2 = N_{\mathrm{CCD}}(\sigma_{\mathrm{CCD}}/\mu)^2$, is equal to the photon shot noise associated with $(n_d)_{min}$. For example, if we assume $n_w = 10^4$ photons pixel$^{-1}$, $\mu = 0.7$, $\sigma_{px} \approx 5$ electrons, $\varsigma_{dk} = 10^3$ electrons s$^{-1}$, $\Delta t = 500\,\mu$s, $m = 1$, and $N = 10^6$, we find that $[(N_{\mathrm{CCD}})_{min}, (N_{\mathrm{CCD}})_{max}] \approx [900, 174 \times 10^3]$. For these pixel numbers and e.g., a CCD size of 13.3 mm × 13.3 mm, the pixel size should be between 31–443 $\mu$m. These technical requirements on the CCD to reach the atom shot noise limit are achievable in commercial scientific sensors.

## 5. Conclusions

In this work we identified fluorescence simultaneous detection of the AI output clouds by CCD imaging as the optimal detection method which poses the least stringent requirements on the detection beam noise and duration. This detection method also allows one to record the cloud spatial information, which is key for improving future AI designs and sensitivity [19, 24], and to reach the atom shot noise limit. AI detection at the atom shot noise limit can allow the further characterization and reduction of other non-detection noise sources limiting the AI sensitivity e.g., wavefront aberration and Coriolis phase shifts. The atom shot noise limit can then be lowered by using much larger atom numbers than the ones considered in this work, but further detection optimization will be required, given the increased optical densities. Otherwise, the AI sensitivity can be enhanced by other techniques, such as the use of large area interferometers with large momentum transfer beam splitters [27] or the use of squeezed atomic states [28], and can reach sensitivities below the classical atom shot noise limit. Thus AI, with high sensitivity at or below the atom shot noise limit, will open new science frontiers such as tests of the general relativity equivalence principle on quantum matter [21]. Furthermore, high precision AIs will be the next generation inertial and gravitational sensors used for civil engineering, geophysical exploration, or climate studies, opening up a new range of possible applications.

## Acknowledgements

We thank EPSRC for support of the GGTop project, grant number EP/I036877/1; the Royal Society for the support of E. R. through the International Newton fellowship, grant NF110071; and UKSA for support of STE-QUEST, grant number ST/K006479/1. We also thank Andrew Hinton, Alexander Niggebaum, Jon Goldwin, and Plamen Petrov for useful discussions and critical reading of the manuscript.

## Appendix A. Full expression of $n_d$ for simultaneous and sequential imaging

For fluorescence detection, the expression of the number of scattered photons $n_s$ reaching the photo detector during a time interval $\Delta t$ is given as a function of the atom number $N$ by:

$$n_s(\nu) = \frac{\Delta t}{h\nu} \int_V \int_{-\infty}^{+\infty} \int_{-\infty}^{+\infty} I(\nu, \vec{r})\sigma\rho(\vec{r})g(v, \vec{r})dVdvd\nu, \tag{A.1}$$

where $\rho(\vec{r})$ and $g(v, \vec{r})$ are the atom density and velocity distributions at the position $\vec{r}$ integrated over a volume $V$ [29], $I(\nu, \vec{r})$ is the laser intensity at frequency $\nu$ and at the position $\vec{r}$, and $\sigma$ is the scattering cross section, which includes power broadening and doppler shifted

detuning. Assuming a two-level atom, $\sigma$ is given by:

$$\sigma = \sigma_0 \left( 1 + 4\frac{(\Delta + \nu v/c)^2}{\Gamma^2} + \frac{I\,(\nu\,(1 + v/c))}{I_{sat}} \right)^{-1}, \tag{A.2}$$

with $\Delta$ the detuning with respect to the resonant frequency $\nu_0$ for the atom at rest, $\Gamma$ the FWHM of the considered transitions, $v$ the velocity of the atoms relative to the laser source, and $\sigma_0$ the on-resonant cross section given by the expression [25]:

$$\sigma_0 = \frac{h\nu}{2}\frac{\Gamma}{I_{sat}}. \tag{A.3}$$

The saturation intensity $I_{sat}$ is defined as in [23, 25] and given by:

$$I_{sat} = \frac{c\varepsilon_0\Gamma^2\hbar^2}{4\left|\hat{\varepsilon}\cdot\boldsymbol{d}\right|^2}, \tag{A.4}$$

with $\hat{\varepsilon}$ the unit polarization vector of the light field and **d** the atomic dipole moment. The various expressions of $I_{sat}$ for different light polarizations can be found in [23].

We assume that the laser source is at rest with respect to the centre of mass of the atom cloud, that there is no atom velocity spread (and so no doppler broadening), and that the laser intensity is constant over the cloud, $I\,(\nu, \vec{r}) = I$. Under these conditions, equation (A.1) becomes:

$$n_s = N\gamma_d\frac{\Gamma}{2}\frac{I}{I_{sat}}\Delta t. \tag{A.5}$$

Then $(\Delta t_{min})_{2l}$ of equation (6) is derived by solving the equation $n_s[(\Delta t_{min})_{2l}]\Omega = (n_d)_{min}$ with $(n_d)_{min}$ from section 2.

If the atom model is not the simple two-level one, but the one represented in figure 3, the expression of $n_d$ has to include as well the possibility of atom loss to closed transitions. In this extended model, the scattered photon number $n_s$ is found by solving the following system:

$$\frac{dn_s}{dt} = \left(N - n_l\right)\frac{I\sigma_0}{h\nu}\gamma_d \tag{A.6}$$

$$\frac{dn_l}{dt} = \left(N - n_l\right)\frac{I\sigma_0}{h\nu}\gamma_{lost}, \tag{A.7}$$

with $n_l$ the number of atoms lost to the alternative hyperfine transitions $\gamma_\mathrm{d}$ and $\gamma_\mathrm{lost}$ as defined for equation (2). Because in this work we assume that all the light polarizations are present and that all the degenerate $m_F$ levels are equally occupied, this multilevel model does not include the optical pumping of the atoms to different $m_F$ levels by the detection beam. Also, the effect of stimulated emissions to lost transitions has not been modeled, since, for small detuning $\Delta$, they represent a second order correction only.

For this multilevel model, $n_s$ as a function of the atom number $N$ is given by:

$$n_s(t) = \frac{N\gamma_d}{\gamma_{lost}}\left(1 - \exp\left(-t\frac{I}{2I_{sat}}\Gamma\gamma_{lost}\right)\right). \tag{A.8}$$

As for two-level system, the minimum detection time $\Delta t_{min}$ to reach the atom shot noise of equation (2) is derived by solving the equation $n_s(\Delta t_{min})\Omega = (n_d)_{min}$.

## Appendix B. Derivation of cross shadowing effect

We model the effect of section 3.2.2 by deriving the scattered photon number $n_s$ in the case of cross cloud shadowing. As in appendix A, we assume no atom velocity spread (so no doppler shift) and a very narrow laser line width, but the detection beams can have variable light density $I_b$ across $x$, $y$, and $z$ due to the shadowing effect. As in figure 9, the laser beam axis is taken parallel to the $z$ axis and retro reflected on a mirror on one side of the clouds. If $I$ is the incoming beam, for small saturation ratio $I/I_{sat}$ or low optical depth [16], the beam exiting from the first cloud is approximatively given by the Beer Lambert Law:

$$I_t(x, y) = I \exp\left(-\sigma\rho_z(x, y)\right) \tag{B.1}$$

$$\approx I\left(1 - \sigma\rho_z(x, y)\right), \tag{B.2}$$

with $\rho_z(x, y)$ the atom number density integrated along the $z$ axis. The total intensity of the laser beams illuminating the first $I_{t1}$ and second $I_{t2}$ cloud are:

$$I_{t1} \approx I\left(2 - \sigma\left(\rho_{1_z}(x, y) + 2\rho_{2_z}(x, y)\right)\right) \tag{B.3}$$

$$I_{t2} \approx I\left(2 - \sigma\left(2\rho_{1_z}(x, y) + \rho_{2_z}(x, y)\right)\right), \tag{B.4}$$

with $\rho_{1z(x,y)}$ and $\rho_{2z(x,y)}$ the $z$ integrated atom densities of the first and second cloud at the AI output. We assume that $\rho_1(x, y, z) = \rho(x, y, z)\xi$ and $\rho_2(x, y, z) = \rho(x, y, z)(1 - \xi)$, that $\rho(x, y, z)$ is normally distributed with standard deviations $\sigma_\rho$ and volume integral $N$, and that the clouds are at a far distance $\gg 2\sigma_\rho$ from each other. The parameter $\xi$ is the probability that each atom will be in the ground state associated with the first output cloud, and it is related to the AI phase $\phi$ being $\xi = (1 + \cos(\phi))/2$. Therefore, the scattered photon numbers for the two clouds are:

$$n_{1s} = \frac{\Delta t}{h\nu}\sigma I\xi \int_{-\infty}^{+\infty} \rho(\vec{r})\left(2 - \sigma\rho(\vec{r})(2 - \xi)\right)\left(1 - \xi g_\rho(\vec{r})\right)dV \tag{B.5}$$

$$= \frac{\Delta t}{h\nu}\sigma 2I\xi N(1 - \tau + \xi(2 - \xi)\Lambda) \tag{B.6}$$

$$n_{2s} = \frac{\Delta t}{h\nu}\sigma I(1 - \xi) \int_{-\infty}^{+\infty} \rho(\vec{r})\left(2 - \sigma\rho(\vec{r})(1 + \xi)\right)\left(1 - (1 - \xi)g_\rho(\vec{r})\right)dV \tag{B.7}$$

$$= \frac{\Delta t}{h\nu}\sigma 2I(1 - \xi)N(1 - \tau + (1 - \xi)(1 + \xi)\Lambda), \tag{B.8}$$

where we included as well the self shadowing of each cloud, and $g_\rho(\vec{r})$, $\tau$, and $\Lambda$ are given by:

$$g_\rho(\vec{r}) = \int_z^{+\infty} \sigma\rho(x, y, \zeta)d\zeta \tag{B.9}$$

$$\tau = \frac{\sigma N}{4\pi\sigma_\rho^2} = 2\rho_{2\,MAX}\,\sigma \tag{B.10}$$

**Table C1.** Branching ratio to closed transition for various alkali elements. $^{7}$Li,$^{23}$Na,$^{39}$K, and $^{41}$Khave the same branching ratio as $^{87}$Rb.

| Element | Transition | br | Element | Transition | br |
|---|---|---|---|---|---|
| $^{87}$Rb | $F' = 2 \rightarrow F = 1$ | 50% | $^{6}$Li | $F' = 3/2 \rightarrow F = 1/2$ | 55.6% |
| $^{87}$Rb | $F' = 1 \rightarrow F = 1$ | 83.3% | $^{6}$Li | $F' = 1/2 \rightarrow F = 1/2$ | 83.9% |
| $^{85}$Rb | $F' = 3 \rightarrow F = 2$ | 44.4% | $^{133}$Cs | $F' = 4 \rightarrow F = 3$ | 41.7% |
| $^{85}$Rb | $F' = 2 \rightarrow F = 2$ | 77.8% | $^{133}$Cs | $F' = 3 \rightarrow F = 3$ | 75% |

$$\Lambda = \frac{N^2\sigma^2}{96\pi^{5/2}\sigma_\rho^5}. \tag{B.11}$$

We substitute equations (B.6) and (B.8) in the definition of $\zeta_m$, and $\delta_\zeta$, obtaining the expression of the shadowing error induced on the population estimate of the AI output clouds of equation (11).

## Appendix C. The spontaneous decay branching ratio

The spontaneous decay branching ratio from a hyperfine level $F'$ of a exited state $J'$ to a hyperfine level $F$ of a ground state $J$ is given by the following equation as a function of Wigner $3-j$, and $6-j$ symbols [25, 30]:

$$\begin{aligned} \mathrm{br}_{\mathrm{F}\rightarrow\mathrm{F}} &= \frac{\Gamma_{\mathrm{F}\rightarrow\mathrm{F}'}}{\sum_F \Gamma_{F\rightarrow F'}} \\ &= (2F+1)(2J'+1)\begin{Bmatrix} J & J' & 1 \\ F' & F & I \end{Bmatrix}^2 \cdot \sum_{q,m'_F}\begin{pmatrix} F' & 1 & F \\ m'_F & q & -m_F \end{pmatrix}^2, \end{aligned} \tag{C.1}$$

where we sum over the possible polarization of the light ($q = -1, 0, 1$) and the hyperfine $m'_F$ sub levels of $F$, and $m_F$ is equal to $m'_F + q$. The previous equation can be found from the expression of the decay rate from a hyperfine level $F'$ of an exited state $J'$ to a hyperfine level $F$ of a ground state $J$ [25, 30, 31]:

$$\Gamma_{F\rightarrow F'} = \sum_{q,m'_F} \frac{\omega_0^3}{3\pi\varepsilon_0\hbar c^3}\left|\left\langle F\left(m'_F+q\right)\left|er_q\right|F'm'_F\right\rangle\right|^2. \tag{C.2}$$

By using the Wigner–Eckart theorem [25, 32] in the previous expression and then by summing $\Gamma_{F\rightarrow F'}$ over all the final ground levels $F$ in equation (C.1), equation (C.1) is derived. For completeness in table C1, we present the branching ratio to closed transition for some alkali atoms and see how they are very similar across different elements.

## References

[1] Raab E L, Prentiss M, Cable A, Chu S and Pritchard D E 1987 Trapping of neutral sodium atoms with radiation pressure *Phys. Rev. Lett.* **59** 2631–4

[2] Kasevich M and Chu S 1991 Atomic interferometry using stimulated Raman transitions *Phys. Rev. Lett.* **67** 181–4

[3] Weiss D S, Young B C and Chu S 1993 Precision measurement of the photon recoil of an atom using atomic interferometry *Phys. Rev. Lett.* **70** 2706–9
[4] Bouchendira R, Cladé P, Guellati-Khélifa S, Nez F and Biraben F 2011 New determination of the fine structure constant and test of the quantum electrodynamics *Phys. Rev. Lett.* **106** 080801
[5] Lamporesi G, Bertoldi A, Cacciapuoti L, Prevedelli M and Tino G M 2008 Determination of the Newtonian gravitational constant using atom interferometry *Phys. Rev. Lett.* **100** 050801
[6] Fixler J B, Foster G T, McGuirk J M and Kasevich M A 2007 Atom interferometer measurement of the Newtonian constant of gravity *Science* **315** 74–77
[7] Fray S, Diez C A, Hänsch T W and Weitz M 2004 Atomic interferometer with amplitude gratings of light and its applications to atom based tests of the equivalence principle *Phys. Rev. Lett.* **93** 240404
[8] Bonnin A, Zahzam N, Bidel Y and Bresson A 2013 Simultaneous dual-species matter-wave accelerometer *Phys. Rev.* A **88** 043615
[9] Gaaloul N, Ahlers H, Schulze T, Singh Y, Seidel S, Herr W, Ertmer W and Rasel E 2010 Quantum tests of the equivalence principle with atom interferometry *Acta Astronautica* **67** 1059–62
[10] Graham P W, Hogan J M, Kasevich M A and Rajendran S 2013 New method for gravitational wave detection with atomic sensors *Phys. Rev. Lett.* **110** 171102
[11] Perl M L and Mueller H 2010 Exploring the possibility of detecting dark energy in a terrestrial experiment using atom interferometry arXiv:1001.4061v1
[12] Geiger R *et al* 2011 Detecting inertial effects with airborne matter-wave interferometry *Nat. Commun.* **2** 474
[13] Muller T, Gilowski M, Zaiser M, Berg P, Schubert C, Wendrich T, Ertmer W and Rasel E M 2009 A compact dual atom interferometer gyroscope based on laser-cooled rubidium *Euro. Phys. J.* D **53** 273–81
[14] Angelis M D *et al* 2011 iSense: a portable ultracold-atom-based gravimeter *Procedia Comput. Sci.* **7** 334–6
[15] Sorrentino F, Bodart Q, Cacciapuoti L, Lien Y H, Prevedelli M, Rosi G, Salvi L and Tino G M 2013 Sensitivity limits of a Raman atom interferometer as a gravity gradiometer *Phys. Rev.* A **89** 023607
[16] Pappa M, Condylis P C, Konstantinidis G O, Bolpasi V, Lazoudis A, Morizot O, Sahagun D, Baker M and von Klitzing W 2011 Ultra-sensitive atom imaging for matter-wave optics *New J. Phys.* **13** 115012
[17] Biedermann G W, Wu X, Deslauriers L, Takase K and Kasevich M A 2009 Low-noise simultaneous fluorescence detection of two atomic states *Opt. Lett.* **34** 347–9
[18] Sorrentino F, Bodart Q, Cacciapuoti L, Lien Y H, Prevedelli M, Rosi G, Salvi L and Tino G M 2014 Sensitivity limits of a Raman atom interferometer as a gravity gradiometer *Phys. Rev.* A **89** 023607
[19] Dickerson S M, Hogan J M, Sugarbaker A, Johnson D M S and Kasevich M A 2013 Multi-axis inertial sensing with long-time point source atom interferometry *Phys. Rev. Lett.* **111** 083001
[20] Müller H, Chiow S, Herrmann S, Chu S and Chung K 2008 Atom-interferometry tests of the isotropy of post-Newtonian gravity *Phys. Rev. Lett.* **100** 031101
[21] Aguilera D N *et al* 2014 STE-QUEST test of the universality of free fall using cold atom interferometry *Class. Quantum Grav.* **31** 115010
[22] Schlippert D, Hartwig J, Albers H, Richardson L L, Schubert C, Roura A, Schleich W P, Ertmer W and Rasel E M 2014 Quantum test of the universality of free fall *Phys. Rev. Lett.* **112** 203002
[23] Steck D A 2009 *Rubidium 87 D Line Data* available online at http://steck.us/alkalidata (revision 2.1.4, 23 December 2010)
[24] Sugarbaker A, Dickerson S M, Hogan J M, Johnson D M S and Kasevich M A 2013 Enhanced atom interferometer readout through the application of phase shear *Phys. Rev. Lett.* **111** 113002
[25] Steck D A *Quantum and atom optics* available online at http://steck.us/teaching (revision 0.9.8, 12 september 2013)
[26] Papoulis A and Pillai S U 2002 *Probability Random Variables and Stochastic Processes with Errata Sheet* 4th edn (New York: McGraw-Hill Higher Education)
[27] Chiow S w, Kovachy T, Chien H C and Kasevich M 2011 102k large area atom interferometers *Phys. Rev. Lett.* **107** 130403

[28] Eckert K, Hyllus P, Bruß D, Poulsen U, Lewenstein M, Jentsch C, Müller T, Rasel E and Ertmer W 2006 Differential atom interferometry beyond the standard quantum limit *Phys. Rev.* A **73** 013814
[29] Tino G M *et al* 2013 Precision gravity tests with atom interferometry in space *Nucl. Phys.* **243–244** 203–17
[30] Metcalf H J and van der Straten P 1999 *Laser Cooling and Trapping* (New York: Springer)
[31] Loudon R 2000 *The Quantum Theory of Light* 3rd edn (Oxford: Oxford University Press)
[32] Brink D M and Satchler G R 1994 *Angular Momentum* (Oxford: Oxford University Press)